X-620-72-486
PREPRINT

NASA TM X- 66150

ATMOSPHERIC AND SURFACE PROPERTIES OF MARS OBTAINED BY INFRARED SPECTROSCOPY ON MARINER 9

DECEMBER 1972

GSFC
GODDARD SPACE FLIGHT CENTER
GREENBELT, MARYLAND

X-620-72-486
Preprint

ATMOSPHERIC AND SURFACE PROPERTIES OF MARS OBTAINED BY INFRARED SPECTROSCOPY ON MARINER 9

December 1972

GODDARD SPACE FLIGHT CENTER
Greenbelt, Maryland

ATMOSPHERIC AND SURFACE PROPERTIES OF MARS OBTAINED BY INFRARED SPECTROSCOPY ON MARINER 9

B. Conrath, R. Curran, R. Hanel, V. Kunde,
W. Maguire, J. Pearl, J. Pirraglia and J. Welker
Goddard Space Flight Center
T. Burke
Jet Propulsion Laboratory

ABSTRACT

During the eleven month operational lifetime of Mariner 9, the infrared spectroscopy experiment obtained data over a large portion of Mars. Between June and October 1972 improvements have been made in the CO_2 transmittances, which are necessary for the interpretation of the thermal emission spectra. Recently obtained spectra indicate that strong seasonal variations in the water vapor distribution over both polar regions occurred. The wettest atmospheric conditions observed so far contain 20-30 precipitable μm of water over the North Polar Cap during northern spring. A low resolution pressure map is presented which covers that portion of the planet between latitudes -60° and +25°. A more detailed study of the Coprates Canyon indicates that at its lowest point the canyon floor must be at least 5 km below the rim. Applications of tidal theory to temperature fields derived from the spectra indicate diurnal surface pressure flucutations of as much as 12% during the Great Dust Storm of 1971-72. Qualitative arguments based on radiative transfer calculations for model dust clouds composed of spherical quartz particles suggest that particle radii during the storm were of the order of a few μm; a complete specification of particle parameters must await the development of more refined models.

ATMOSPHERIC AND SURFACE PROPERTIES OF MARS OBTAINED BY INFRARED SPECTROSCOPY ON MARINER 9

INTRODUCTION

The infrared spectroscopy experiment on Mariner 9 obtained data over much of Mars during the eleven month operational lifetime of the spacecraft. Thermal emission spectra have been recorded by the Michelson interferometer from 200 to 2000 cm^{-1} (50 to 5 μm) with a spectral resolution of 2.4 cm^{-1} in the apodized mode of data reduction. The spatial resolution corresponds to a circular area of 125 km diameter at periapsis and vertical viewing but changes with spacecraft — Mars distance. A noise equivalent radiance of 0.5×10^{-7} watt cm^{-2} sr^{-1} $/cm^{-1}$ has been deduced from the repeatability of the calibration spectra taken periodically from deep space and from a built-in blackbody. The calibration spectra also indicated constancy of the responsivity of the instrument between prelaunch tests and end of mission.

The scientific objectives of the experiment include the interpretation of the thermal emission of Mars in terms of atmospheric temperatures, wind fields and dynamics, surface temperatures, surface pressure and topography, mineral composition, and minor atmospheric constituents including isotopic ratios, as well as a search for unexpected phenomena. The derived physical parameters may also be pertinent to biological investigations. The availability of a large and continuous portion of the spectrum permits flexibility in designing methods of interpretation and allows analysis of unforeseen phenomena.

The latter was well demonstrated by the significance of information extracted from spectra obtained during the unexpectedly violent dust storm.

The scientific goals of the infrared spectroscopy experiment as established in advance of the mission have been discussed (Hanel et al., 1970); a description of the Fourier transform spectrometer used in this experiment has been given (Hanel et al., 1972a); and first results and interpretation of the data up to May 1972 have been published (Hanel et al., 1972b, 1972c). The purpose of this paper is to report on analysis of the data carried out from June through October 1972. The data analysis is far from complete so the paper is necessarily a progress report on ongoing work.

CARBON DIOXIDE AND WATER VAPOR TRANSMITTANCES

Fundamental to the quantitative interpretation of planetary emission spectra is a precise knowledge of the transmittances of atmospheric gases present: in this case primarily carbon dioxide and water vapor.

In addition to providing the basis for analysis of atmospheric temperatures and surface pressure, the CO_2 transmittances are also required to estimate isotopic abundances of carbon and oxygen, and to allow identification of other gaseous constituents in the spectral range covered by the instrument. Refinement of the CO_2 transmittances as a function of wave number, temperature and pressure has continued. In order to assess the validity of the theoretical transmittances and as a check on the internal consistency of the techniques used for the retrieval of surface pressure and atmospheric temperatures, a

synthetic Martian spectrum has been calculated using a line by line integration technique (Kunde, 1968). Molecular absorption by CO_2 and H_2O is included in this theoretical model. The computed spectrum is based on a solution of the equation of radiative transfer and uses the surface pressure and temperature profile derived from portions of the same set of spectra for which the comparison is made. Because the operational computer program which derives surface pressure and atmospheric temperatures uses a parameterized form of the CO_2 transmittances which is not as precise as the line by line integration technique, small differences between the computed and the experimental radiances are expected. Use of parameterized transmittances is dictated by the great expense in computer time required by the line by line integration method for processing individual spectra.

Observed spectra were chosen from revolution 174 near local noon and near the sub-solar latitude to maximize the thermal contrast, thereby enhancing the appearance of spectral features. Eighteen spectra were averaged to reduce the random noise to approximately 1×10^{-8} watt cm^{-2} sr^{-1} $/cm^{-1}$. While this noise-equivalent-radiance is approximately independent of wavenumber, the corresponding noise-equivalent-temperature varies from less than 0.7K at 300 cm^{-1}, to less than 0.1K at 800 cm^{-1}, to less than 0.6K at 1600 cm^{-1}.

The 200-500 cm^{-1} and the 500-800 cm^{-1} regions, respectively, of the average measured brightness temperature are compared with theoretical spectra in Figures 1 and 2. The theoretical spectra were computed using the

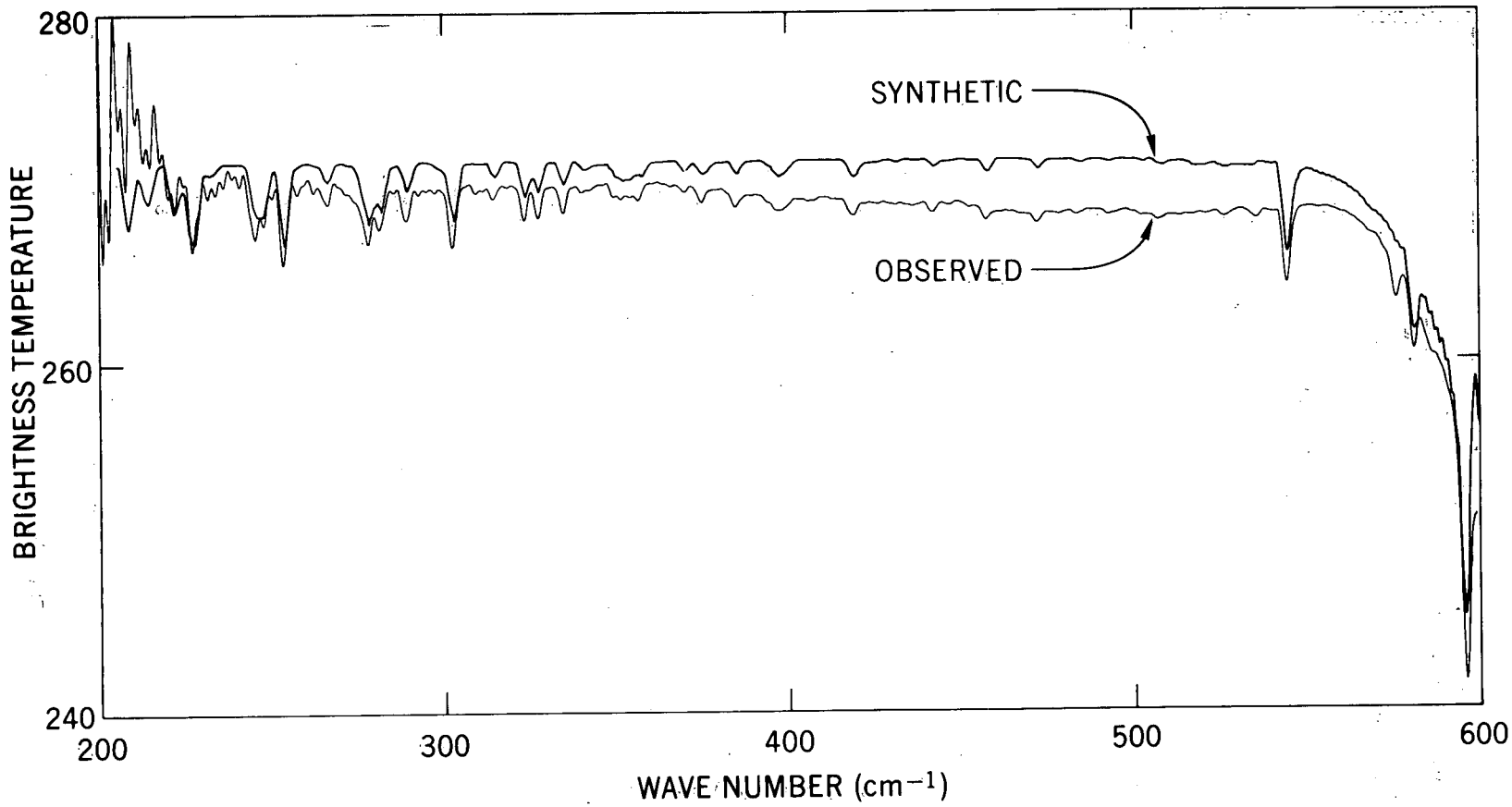

Figure 1. Comparison of synthetic and observed spectra for Rev. 174 (-30° lat., 32° long., 14:00 local time) in the region of absorption by atmospheric water vapor. The synthetic spectrum contains 10 μm of precipitable water vapor.

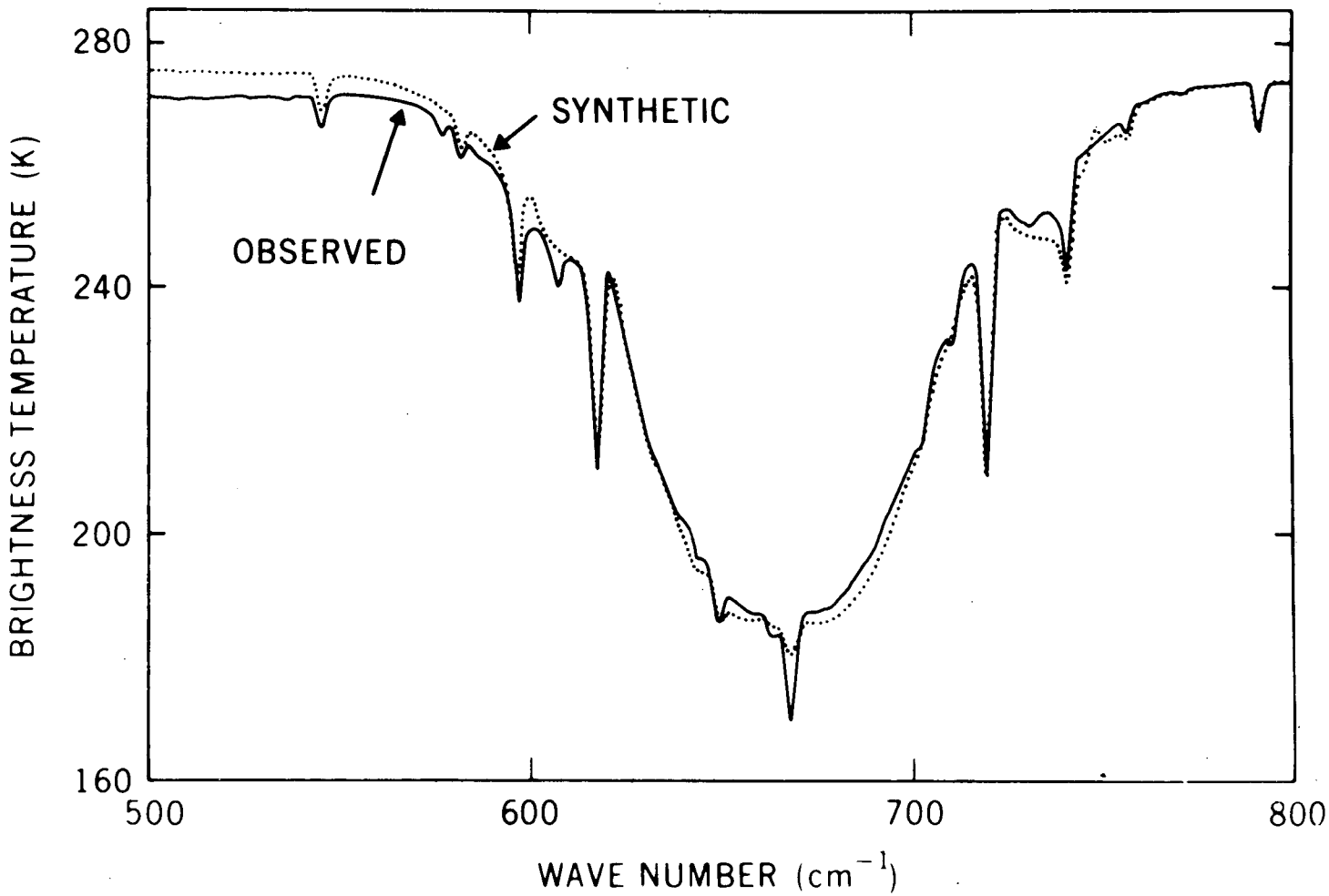

Figure 2. Comparison of synthetic and observed spectra for Rev. 174 (30° lat., 32° long., 14:00 local time) in the region of absorption by atmospheric carbon dioxide. Numerous Q-branch features of individual CO_2 bands, superimposed on the strong absorption by the CO_2 fundamental at 667 cm^{-1}, are evident in the observed spectrum.

surface pressure and vertical temperature profile retrieved from the radiances in the 668-750 cm^{-1} region and a total water vapor content of 10 precipitable μm as determined from the H_2O lines in the 250-325 cm^{-1} region. The H_2O line parameters were from Benedict and Kaplan (Private Communication, 1967) while the CO_2 parameters were generated from band positions and band strengths obtained from Benedict (1970) and from Drayson (1972). Numerous rotational absorption lines, due to atmospheric H_2O are evident in the 200-500 cm^{-1} regions shown in Figure 1. The comparison of the observed and the theoretical spectrum shows good spectral correspondence between the known H_2O lines, even for the weak lines in the 500 cm^{-1} region. No unidentified or anomalous features are evident in this spectral interval.

Strong molecular absorption by atmospheric CO_2 appears between 500 and 800 cm^{-1} as shown in Figure 2. Several of the strongest CO_2 bands for the five most common isotopes are listed in order of descending band strength in Table 1. The band strengths for the isotopes have been determined from the corresponding $O^{16}C^{12}O^{16}$ band strength scaled in accordance with terrestrial isotopic abundances (Handbook of Chemistry and Physics, 1971). The very weak bands enclosed by the dashed line in the right hand corner do not appear in the available laboratory CO_2 spectra, so their molecular parameters are not readily available. Consequently, these bands were not included in the present computations.

Some of the stronger CO_2 bands observed in the 667 cm^{-1} region of the Martian spectra are given in Table 2. A search has been made for isotopes of carbon dioxide in the Martian infrared spectra, but the identification of bands belonging to other than the main isotope is hindered by their relative weakness. Nevertheless, the $O^{16}C^{13}O^{16}$ fundamental is observed at 648.52 cm^{-1}, the $O^{16}C^{13}O^{18}$ fundamental at 643.49 cm^{-1} and the $O^{16}C^{12}O^{18}$ fundamental at 662.32 cm^{-1}. The relative strengths of these observed bands are in general agreement with the corresponding theoretical bands, indicating the C^{12}/C^{13} and O^{16}/O^{18} ratios for Mars are close to the terrestrial values.

Beyond 800 cm^{-1} the observed spectrum exhibits features due to numerous weak CO_2 bands (800-2000 cm^{-1}), to silicate dust (900-1200 cm^{-1}), and to the 1595 cm^{-1} H_2O band (1400-1800 cm^{-1}); a comparison with a synthetic spectrum for this region is not made at this time because of uncertainties in some of the molecular parameters for the weak CO_2 bands and in the theoretical modeling of the silicate dust.

Two related problem areas are apparent from the comparison shown in Figure 2. The first area is concerned with the presence of anomalous spectral features in the observed spectrum which do not appear in the theoretical CO_2 spectrum. The second problem area concerns inaccuracies in the retrieved surface pressure and temperature profiles which in turn, lead to differences between the theoretical and observed spectrum in the 500-800 cm^{-1} region.

The anomalous spectral features include Q-branch type absorptions at 577, 607, 702, and 711 cm^{-1} and a more diffuse feature near 730 cm^{-1}. Because they are highly correlated in appearance with adjacent weak CO_2 bands which are known to be formed in the lower scale height of the atmosphere, the features are inferred to be of atmospheric origin. Their behavior throughout the mission implies that they are produced by an absorber having a constant mixing ratio over the planetary disk. These characteristics strongly suggest that the disagreement is either due to an incomplete theoretical treatment of CO_2 or that CO_2 connected phenomena exist. Several additional very weak bands of CO_2 are shown in Table 1 below and to the right of the dotted line. Because most of the anomalous features are nearly coincident with these weaker CO_2 bands which have not been included in the present computations, it would be premature to speculate on the origin of these features until the CO_2 spectrum can be completely specified. A revised set of CO_2 lines, including many weaker bands, is now under preparation.

The atmospheric molecular transmittances employed in the algorithms for determining surface pressures and atmospheric temperature profiles from the observed radiances in the 667-750 cm^{-1} region currently contain two main sources of error. One source is the theoretical CO_2 absorption parameters which are based mainly on laboratory data obtained at room temperature and terrestrial pressures. Further laboratory CO_2 data, not now available, should be recorded under Martian temperature, pressure and CO_2 path conditions in

order to verify the theoretical CO_2 parameters for the Martian application. A second source of error in the transmittances is the unknown opacity of the anomalous spectral features. The features at 702 and 711 cm^{-1} are of particular concern, since these wavenumbers are close to spectral intervals which are employed in estimating temperature profiles and surface pressures.

WATER VAPOR ABUNDANCE AND DISTRIBUTION

During the dusty mid-summer season in the Southern Hemisphere of Mars, the atmospheric water vapor abundance was approximately 10 to 20 precipitable μm over most of the planet except the northern polar area, where no water vapor could be detected (Hanel et al., 1972c). Additional water vapor estimates based on subsequent data show seasonal and secular effects marked by the disappearance of water vapor over the south polar region, and its appearance in the north polar area.

The total water vapor abundances again were determined from a comparison of synthesized and observed spectra such as those illustrated in Figure 1, assuming the vertical water vapor distribution was well mixed for the early periods, up to revolution 120, and decreased exponentially with a 5 km scale height thereafter.

The water vapor abundances are summarized in the lower three sections of Figure 3 for the North Polar Cap, sub-solar point and South Polar Cap regions with the upper section of the Figure illustrating the classical polar cap regression curves. The cross-hatched areas and upper limit designations,

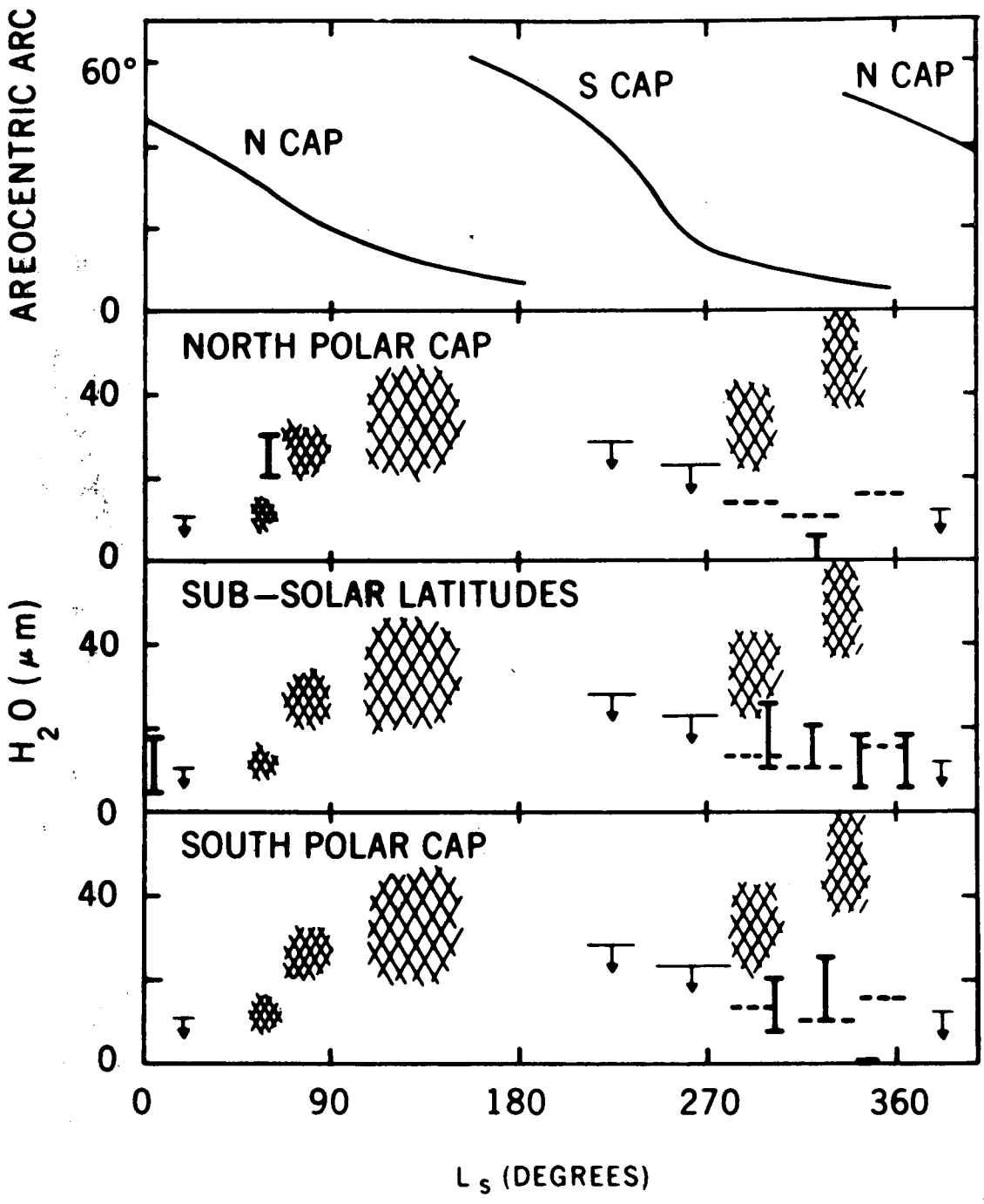

Figure 3. Summary of latitudinal distribution of atmospheric water vapor with changing Martian season.

representing the ground-based water vapor determinations from the 1965 and 1969 oppositions, have been taken from Barker, et al., (1970). The vertical extent of the cross-hatched areas includes the ground-based measured latitudinal differences of water vapor. For convenience the ground-based values are indicated in each of the summary sections. The average abundances for the '71-'72 opposition by Tull and Barker are marked by the dashed lines and represent a measurement over the entire Martian disk. The early conclusions concerning the Martian water vapor were summarized in the previous paper (Hanel, et al., 1972c).

An upper limit to the amount of water vapor which can be observed is determined by the saturation level of the atmosphere, which in turn is strongly controlled by the atmospheric temperatures. Typical temperature profiles for the South Polar Cap and North Polar Cap regions are shown in Figure 4 with the corresponding spacecraft revolution numbers.

The three profiles over the South Polar Cap region cover the last half of a southern summer. The surface pressure was taken at 5 mb (Kliore, 1972). The decrease in atmospheric temperatures between Revolution 30 and Revolution 188 is a consequence of the decreasing solar illumination in the South Polar region as the sub-solar point moves toward the equator with the passage of summer and to the settling of the dust after the storm.

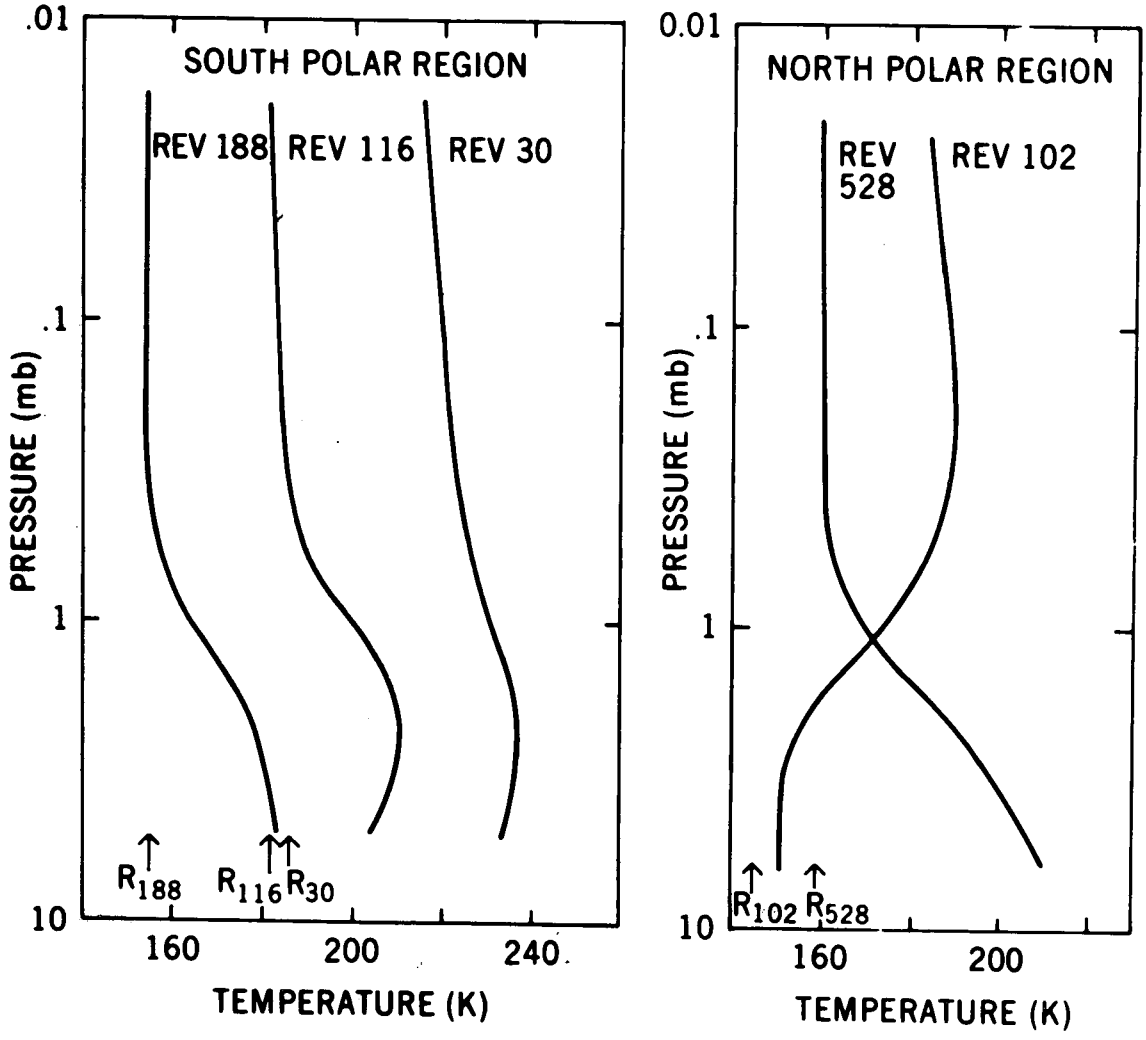

Figure 4. Temperature profiles retrieved from the 667 cm^{-1} CO_2 band summarized for the South Polar Cap region during southern summer and for the North Polar Cap during Northern winter and spring. The arrows near the bottom of the figure indicate the surface temperature measured from the 400 cm^{-1} region of the spectrum.

The temperature profile for Revolution 528, corresponding to late northern spring conditions, manifests the increasing solar illumination. The assumed surface pressure was 6 mb (Kliore, 1972). A summary of the surface pressures (P_{surf}), surface temperatures (T_{surf}) and observed and saturation amounts of atmospheric water vapor (U_{obs} and U_{sat}, respectively) are given in Table 3. The surface brightness temperatures given in the table were derived at 400 cm^{-1}. Due to the fact that the instrument field of view includes both frost covered and clear areas over the Polar caps (Hanel, et al., 1972b), these temperatures are not inconsistent with a CO_2 cap.

Through saturation limits alone, the observed behavior of the South Polar Cap temperature profiles constrains the late summer atmospheric water vapor content to small amounts. For example, the maximum water vapor content for Revolution 188 must be less than 0.7 μm; in fact, water was no longer evident in the spectra of the South Polar Cap area. On Revolution 528, approximately two-thirds through northern spring, the North Polar Cap area showed about 20 to 30 precipitable μm of water vapor which is close to the saturation level at that time. The distribution of water vapor at midlatitudes remained quite stable during the entire mission. On Revolution 261 during early Northern spring over the sub-solar latitudes the abundance was still 10 to 20 precipitable μm.

Further analysis of the water vapor is expected to refine the absolute determination of the abundance, determine a crude scale height, give a more

complete representation of the latitudinal and seasonal distribution, and yield some insight into possible water vapor sources and transport processes.

SURFACE PRESSURE AND TOPOGRAPHY

Surface pressures have been derived for more than 3500 points on the planet where spectra show a large thermal contrast between mean atmospheric temperatures and soil surface temperatures. Data points are generally spaced at intervals of 100-200 km along the instrument ground track; the separation between ground tracks is as much as 600 km. The spatial resolution element of each measurement varies from 125 to 200 km in diameter.

The data have been averaged over areas 5° on a side to provide a low resolution pressure map of the half of the planet between latitudes of -60° and +25° (Figure 5). The average surface pressure over the sampled area is 5.0mb. The highest pressures observed (~8 mb) occur in Hellas and in the Isidis Regio-Amenthes area. Other relatively high pressure regions (~6 mb) are Argyre I and portions of Chryse and Margaritifer Sinus. The Tharsis-Syria plateau is characterized by pressures less than 3.5 mb, with a pressure of 1.5 mb at the top of South Spot (-9°, 120°). Even at the low resolution of this figure, the great Coprates Canyon complex is suggested between 35° and 95° longitude. Correlations with other large features, such as the large crater centered at (-52°, 82°) in southern Bosporos, are also evident.

Martian topography can be obtained from the surface pressure distribution by use of the barometric law. Topographic maps of Hellas and the Tharsis area,

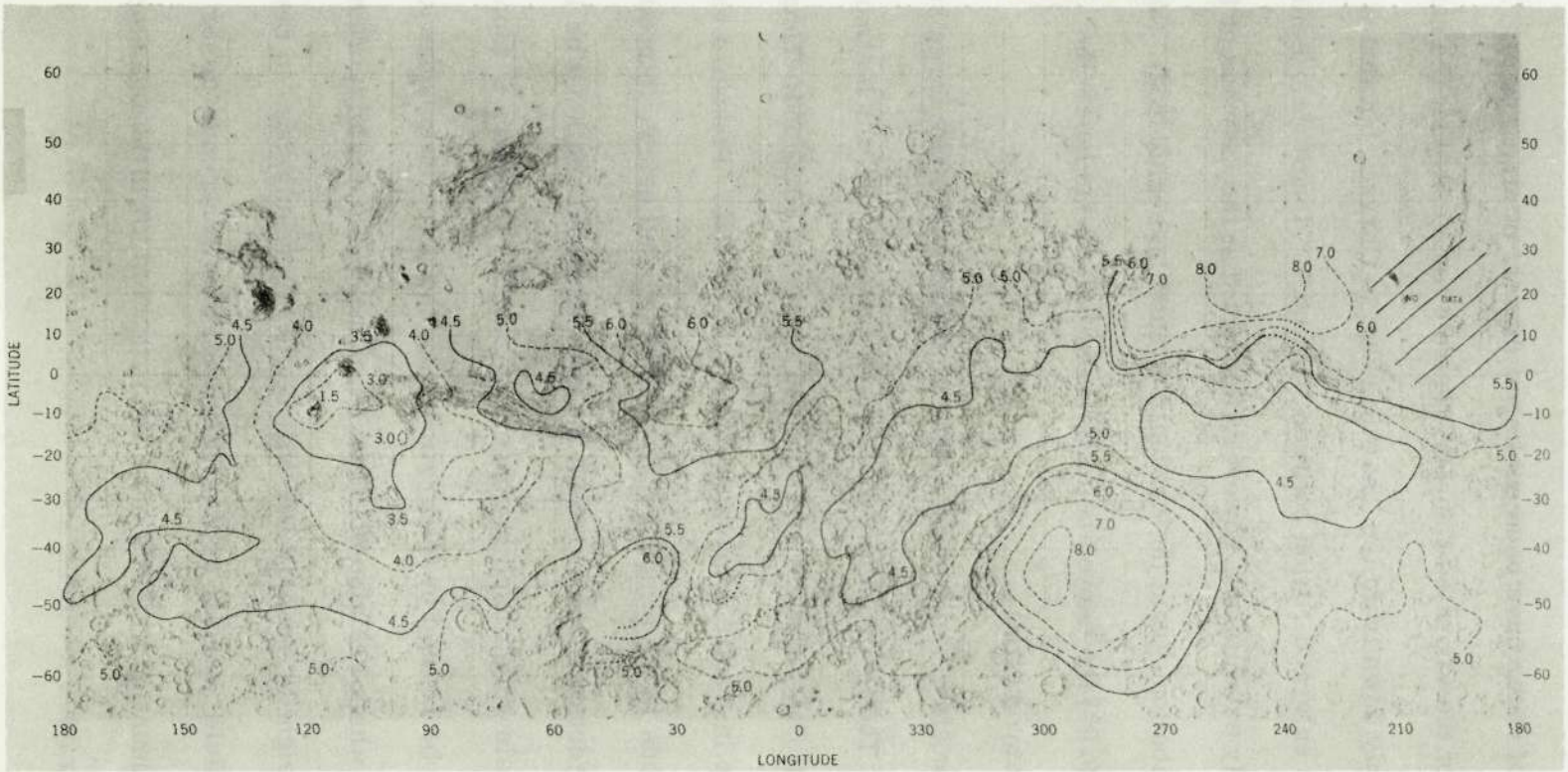

Figure 5. Preliminary pressure map based on pressure averaged over areas 5° on a side. Pressure contours (in millibars) are shown overlaying the feature map produced by the USGS from Mariner 9 TV pictures. Contours corresponding to integer pressure values are dashed, and those corresponding to half integer values are solid. Dotted portions of the contours are interpolated across data gaps. Accuracy of the pressure determinations is 10-15%.

based on an atmospheric scale height of 10 km, and a zero level at the 6.1 mb triple point pressure of water have been published (Hanel, et al., 1972c). A similar investigation of the Coprates Canyon (Figure 6) suggests that the canyon does not slope uniformly down from the Tharsis ridge to Chryse, but that it has a local low area in the enlarged region between 70° and 75° longitude. Before this can be conclusively established, however, the fact that the instrument field of view includes contributions from the canyon rim must be considered. Nevertheless, at (-10.6°, 70.0°) the canyon bottom lies at least 5 km below the southern edge of the canyon rim.

Several systematic effects are being evaluated which will affect large scale topographic mapping. The theoretical CO_2 transmittances from which atmospheric opacity and total CO_2 amounts are obtained are being finalized; changes to the preliminary map in Figure 5 are expected to be 10-15%. Pressure variations due to tidal motions in the atmosphere, to be discussed below, introduce a latitude dependent effect of perhaps 10% in the area sampled and must be included. The 10 km scale height used in converting surface pressure to topographic altitudes must be refined by integrating down the actual atmospheric temperature profiles, which are also obtained from the IRIS data; an increase in the average scale height by roughly 10% will result. Irregularities in the Martian gravitational field (Lorell, et al., 1972) will also contribute minor systematic effects, amounting to shifts of on the order of 1 km in the geopotential surface to which topographic altitudes are referred.

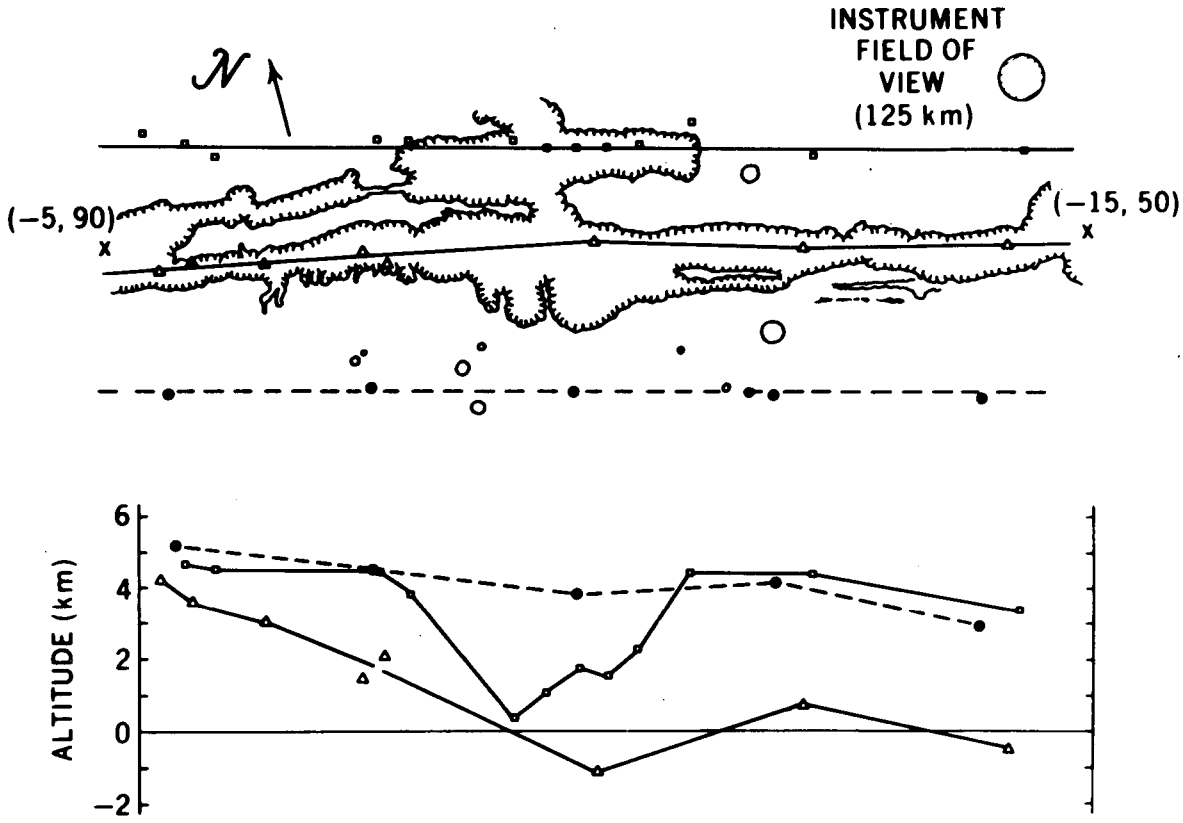

Figure 6. Preliminary topography in Coprates Canyon region. Upper portion of figure shows configuration of the canyon between longitudes 50° and 90°. Data points chosen from several data passes are indicated along three lines closely paralleling the main canyon structure. Lower part of figure shows topography along these lines as obtained from pressure data using a 10 km scale height and an altitude zero at 6.1 mb. The dashed line lies over the generally smooth terrain south of the canyon, and provides a measure of the overall slope of the region. The maximum apparent depth of 5 km is at about longitude 70°; correction for instrument field of view must be made before this can be conclusively established as a local minimum in the canyon structure.

ATMOSPHERIC CIRCULATION

Temperature profiles obtained from measurements in the 667 cm^{-1} CO_2 bands have been employed in the construction of semi-global temperature fields from which preliminary estimates of large-scale winds during the great dust storm of 1971-72 were made (Hanel, et al., 1972c). In that work, the surface pressure was assumed to be constant, surface friction and orographic effects were not included, and non-linear terms in the hydrodynamic equations were neglected. The large diurnal fluctuations observed in the temperature fields imply the existence of strong tidal effects which can appreciably alter the near surface winds; consequently, the second step in a continuing analysis of the wind fields has been the incorporation of tidal theory into the calculations. Tidal theory treats the harmonically varying part of the planetary circulation, taking into account surface pressure fluctuations but neglecting non-linear effects, surface friction and topography.

As in the previous report, the observed temperature field was modeled using a spherical harmonic representation consisting of two meridional harmonics each for zonal wave numbers zero and one. In this way the temperature fields were extrapolated into those regions for which no direct measurements exist, primarily in the night hemisphere. The vertical temperature structure was included by using altitude dependent coefficients for the harmonic terms. The resulting temperature model was used to evaluate the driving terms of the hydrodynamic equations. Unlike more conventional calculations which employ

the heat input to the system as the driving agent, the present wind calculations do not make use of the energy equation directly; instead it can be used to calculate the heat input required to be consistent with the derived motions and observed temperatures. A number of approximations were made to render the hydrodynamic equations tractable, including linearization, the neglect of surface friction and orographic effects, and the assumption of a linear damping term with a four day time constant. With these approximations, the dynamic equations were reduced to an inhomogeneous tidal equation for the surface pressure. Solution of this equation yielded the surface pressure field which, along with the temperature field, was employed in the momentum equations to calculate the tidal winds.

The calculated surface pressure field during the great dust storm is shown in Figure 7. Diurnal tidal pressure fluctuations are found to be approximately 12% of the global average surface pressure. The maximum amplitude occurs at a latitude approximately half-way between the equator and the latitude of the maximum temperature fluctuation; in the absence of damping, the maximum pressure amplitudes would occur nearly on the equator. The pressure minimum occurs in local time near the temperature maximum, but with a slight lag caused by the damping.

Near-surface winds obtained from the calculations are shown in Figure 8 and again in Figure 9 as viewed from the poles. Comparison of these results with the earlier calculations indicates that inclusion of the surface pressure

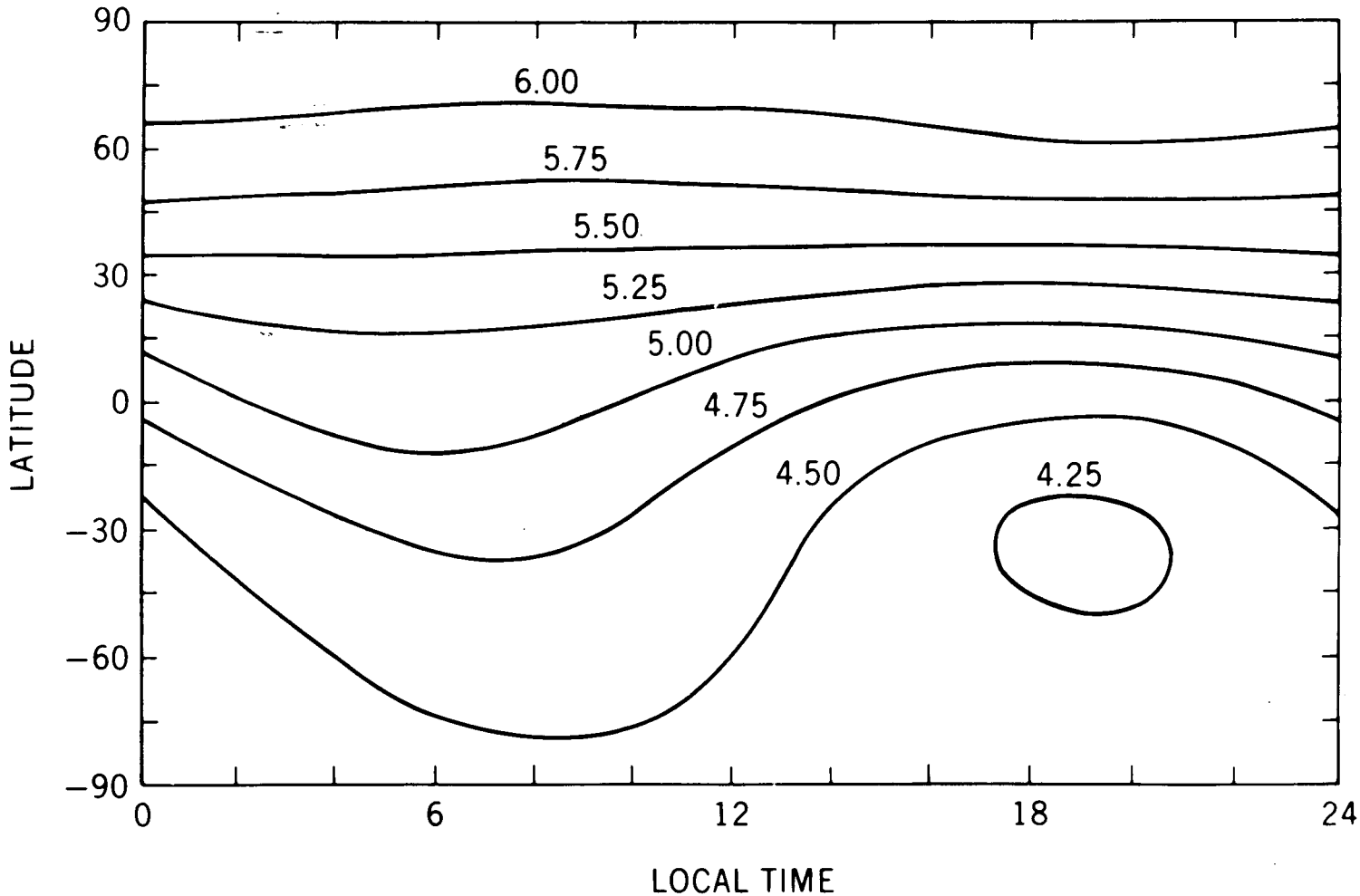

Figure 7. Calculated tidal surface pressure contours. The surface pressures shown are the sum of the diurnal tidal pressures and a latitude dependent seasonal pressure field. The pressure is expressed in millibars and the average surface pressure is 5 mb. Topography and surface friction are not included.

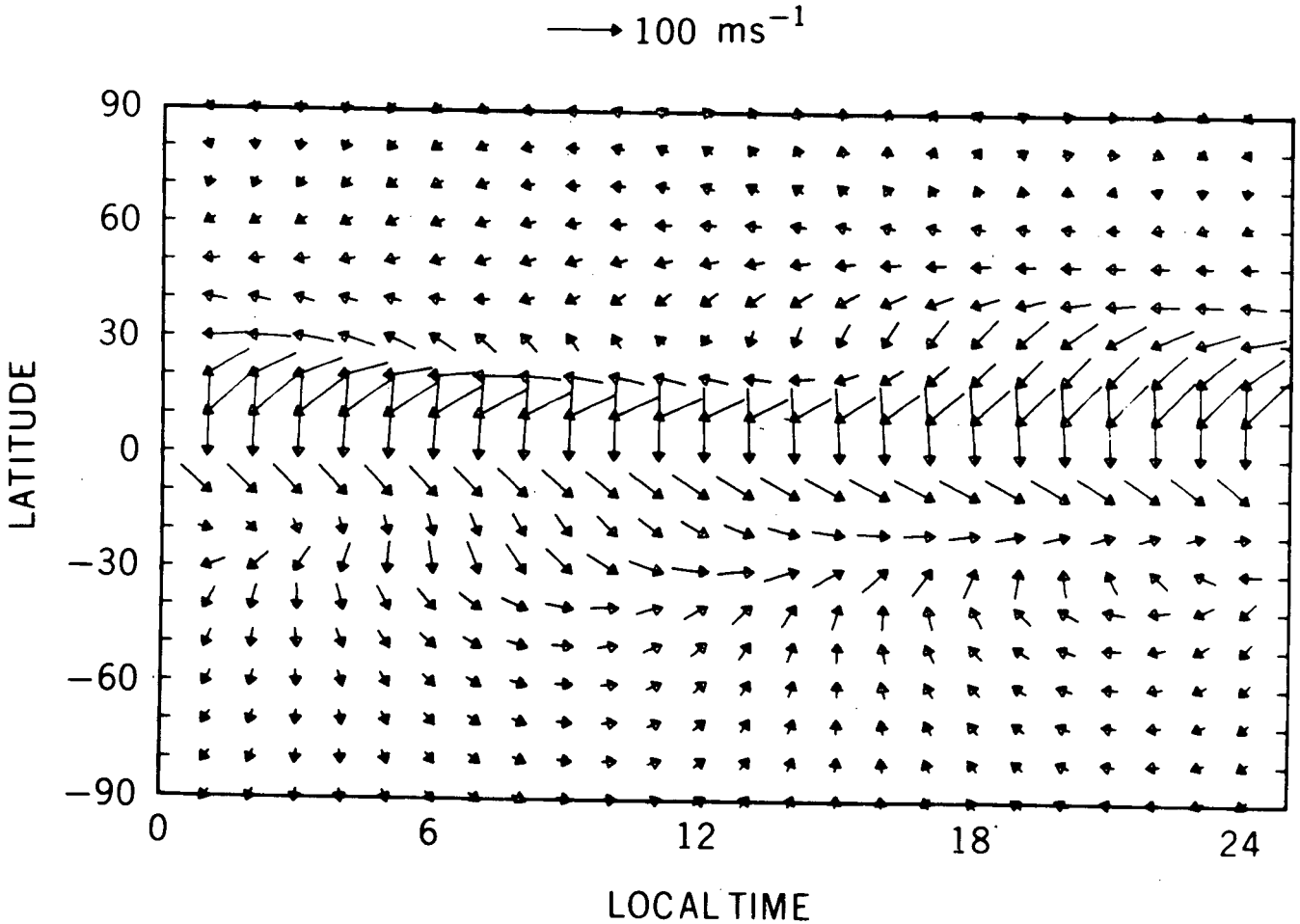

Figure 8. Near surface winds during the great dust storm. The wind field, just above the surface boundary layer, is generated from the measured temperature field and the associated surface pressure. Wind amplitudes are scaled to the labeled vector.

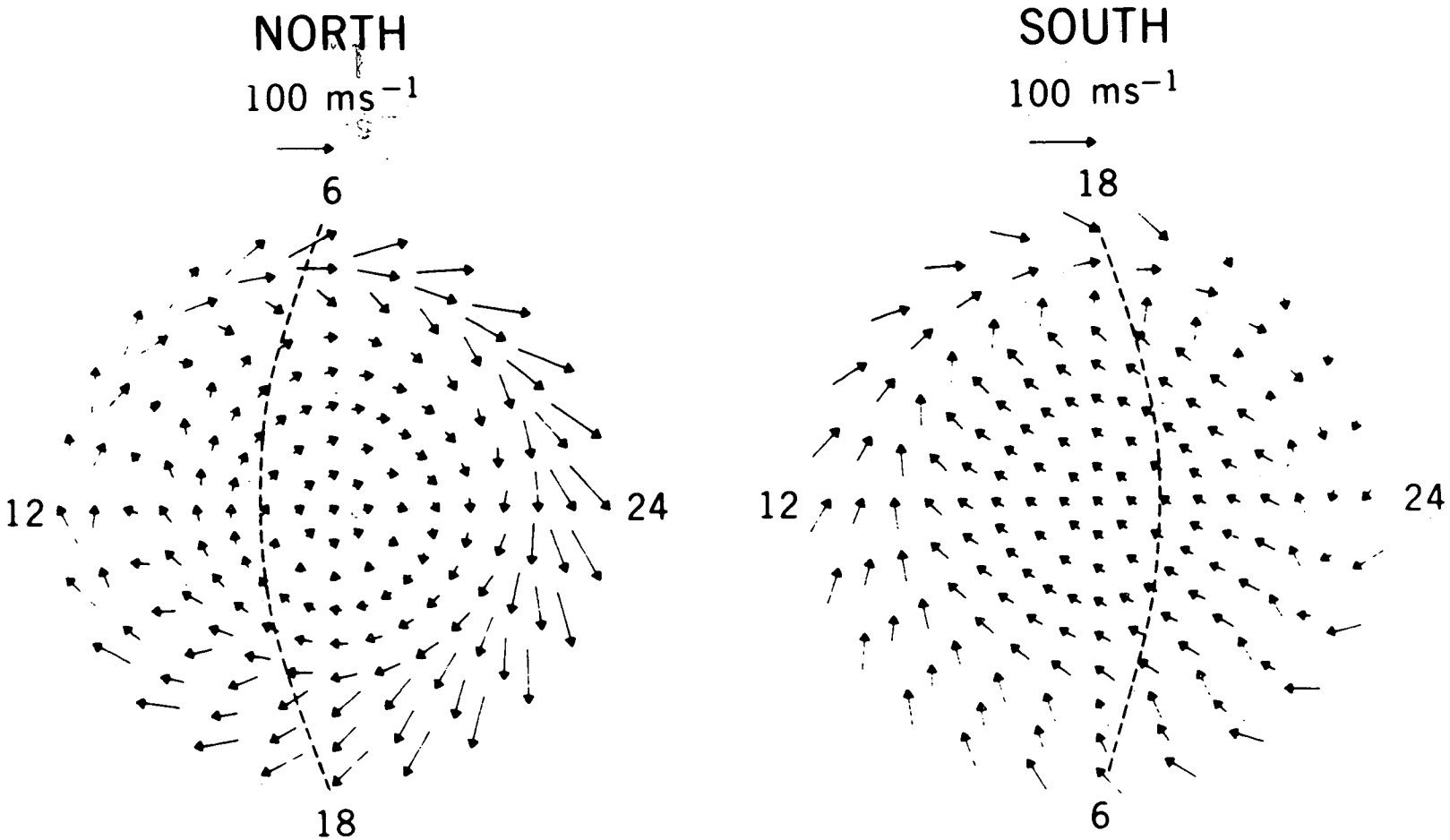

Figure 9. Polar plots of the wind fields of Figure 8. Winds are shown from the poles to within 10° latitude of the equator. The magnitude of the wind velocity is scaled to the labeled vector. The dotted line indicates the position of the terminator.

fluctuations nearly reverses the near-surface wind direction. However, the high altitude wind patterns remain essentially unaffected. Convergence and divergence of the horizontal winds generate vertical winds which cause a diurnal partial overturning of the atmosphere in addition to a seasonal meridional circulation. The magnitudes of the winds shown in Figure 8 near the equator are highly uncertain because of a strong dependence on the amount of damping used and possibly also on non-linear terms which have been neglected. Large-scale topography may significantly alter both the magnitude and direction of the winds at all latitudes. An effort is currently underway to include in the calculations topographic information derived from the surface pressure mapping results.

ATMOSPHERIC DUST

An estimate of the approximate silicon oxide content of the atmospheric dust cloud has been given (Hanel, et al., 1972c). To help further define the properties of the cloud particles a radiative transfer model is being constructed which allows the computation of the emission spectrum of a cloud, between 200 and 2,000 cm^{-1}, given the complex refractive index of the cloud material, the particle size distribution, the number density as a function of height, and the atmospheric temperature profile.

In first tests of this model, the particles were assumed to be quartz spheres of various diameters. Agreement with the measured Martian spectra is not expected to be good since the dust is not pure SiO_2 (quartz) nor is it composed of spherical particles distributed over a narrow range of particle sizes.

Some qualitative conclusions can be reached, however, even though the present computations are primarily a test of the method.

Quartz was chosen because its complex refractive index (Figure 10) is well known (Spitzer and Kleinman, 1961). The Mie theory was assumed to apply, and rectangular particle size distributions were chosen with mean radii at 0.1, 1, 2, 4, and 10 μm. In order to obtain smooth solutions, a width to mean radius ratio of 0.1 was employed in all five cases. Using these distributions, the scattering and absorption cross sections were calculated in a manner similar to that of Peterson and Weinman (1969) for a birefringent material. The cross sections are shown in Figure 11 for particle sizes of 0.1 μm and 10μm. The dominant interaction changes from absorption to scattering as particle size is increased through this range.

Next, the wave number dependent ratios of the total infrared optical depths to the visible optical depth (at 20,000 cm^{-1}) were evaluated. Results for three different particle sizes are shown in Figure 12. It can be seen that the smaller particles tend to interact with the infrared radiation field less efficiently than the larger particles. A comparison of the optical depths for the smaller particles in Figure 12 with the indices of refraction in Figure 10 indicates that maxima in the optical depths correspond to regions of maximum absorption. As the particle size increases, the regions of low absorption in the total optical depth become filled in because of increased scattering; for a particle size of 10μm, scattering dominates as shown in Figure 11, and sharp spectral features are no longer prominent in the total optical depth.

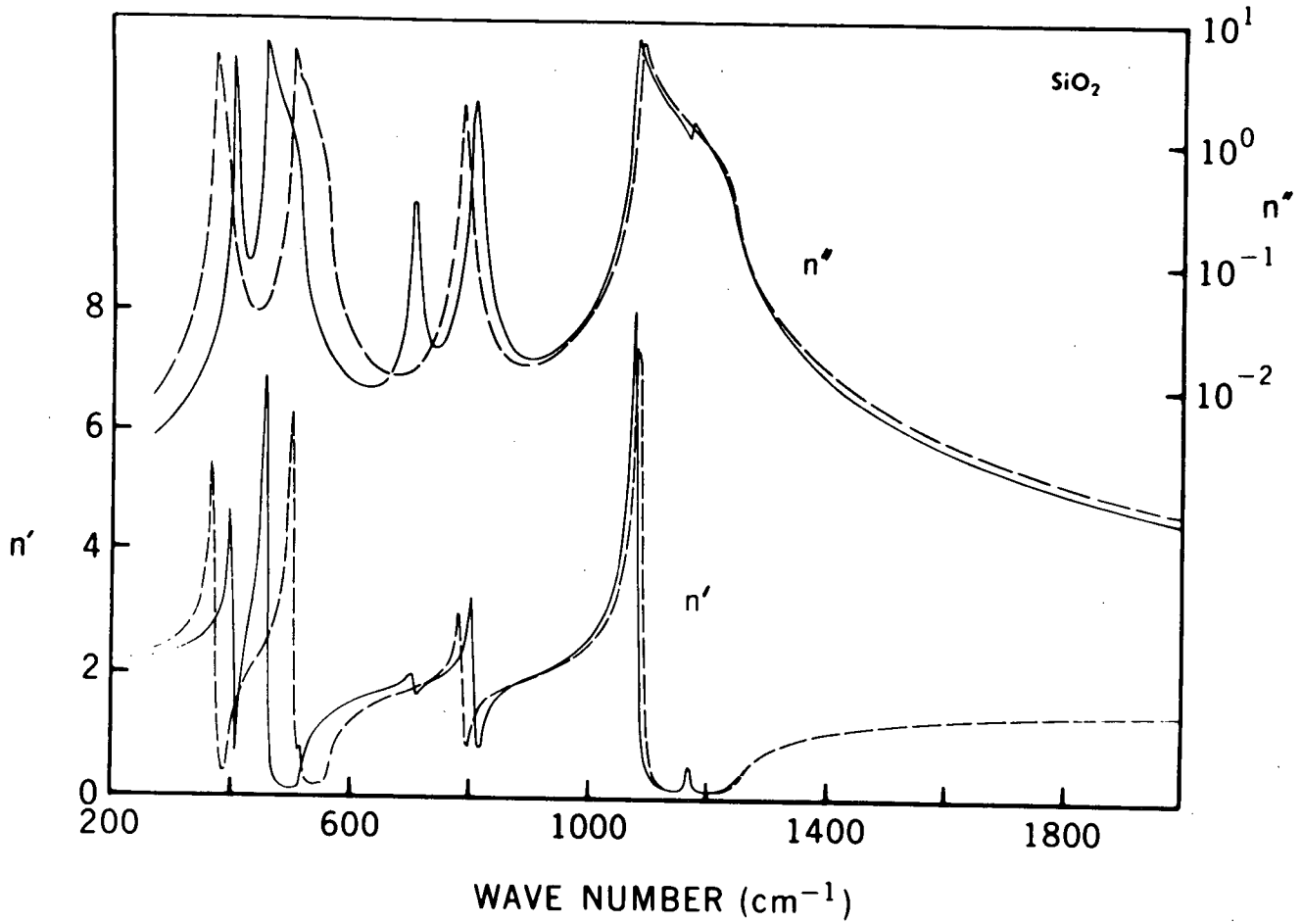

Figure 10. Complex refractive indices of SiO_2 in the infrared. The real part of the refractive index is indicated by n' and the imaginary part by n''. Indices for the ordinary ray are represented by solid lines and for the extraordinary rays by dashed lines.

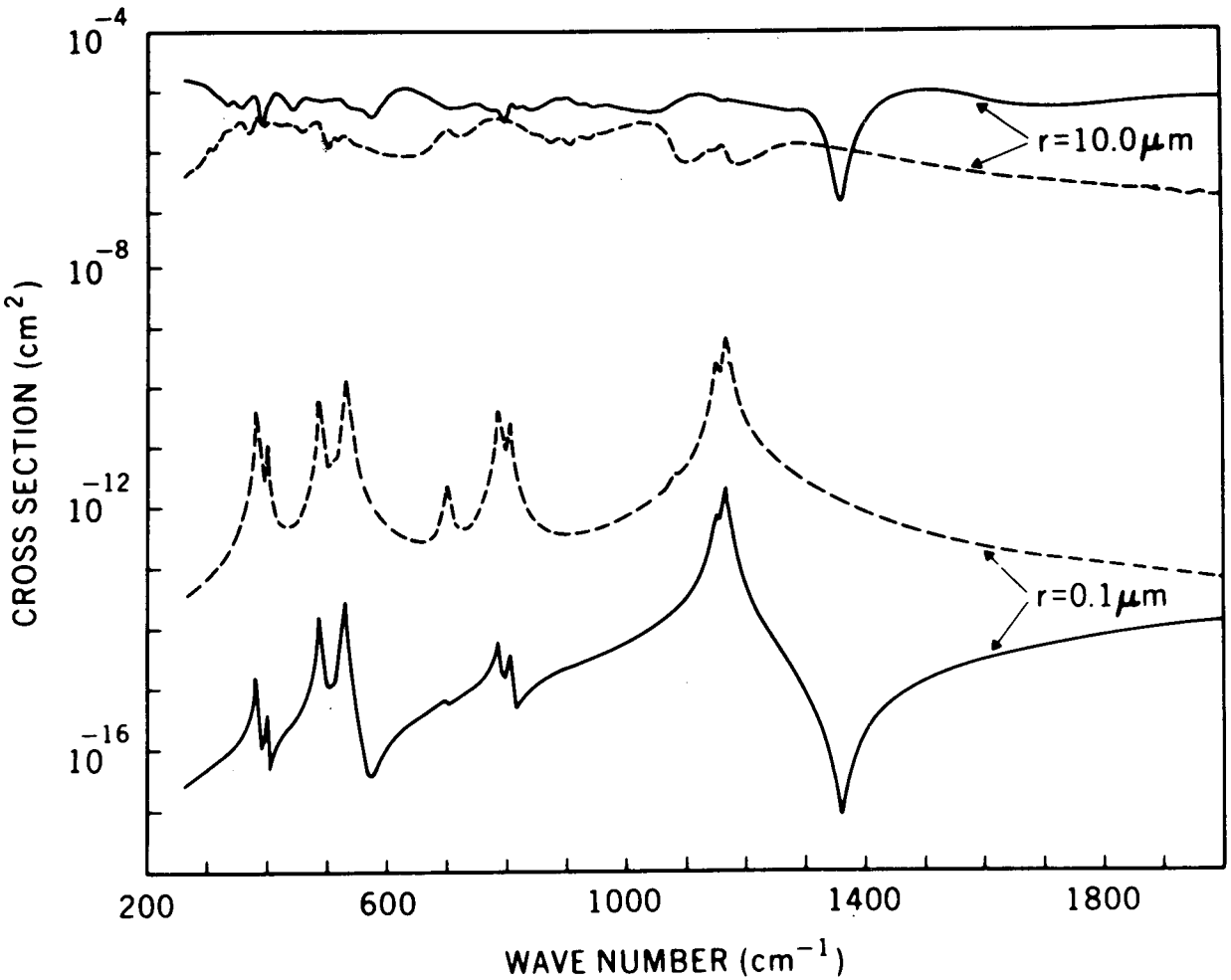

Figure 11. Infrared cross sections for 0.1 μm and 10.0 μm radius particles. The absorption cross sections are indicated by dashed lines and the scattering cross sections by solid lines.

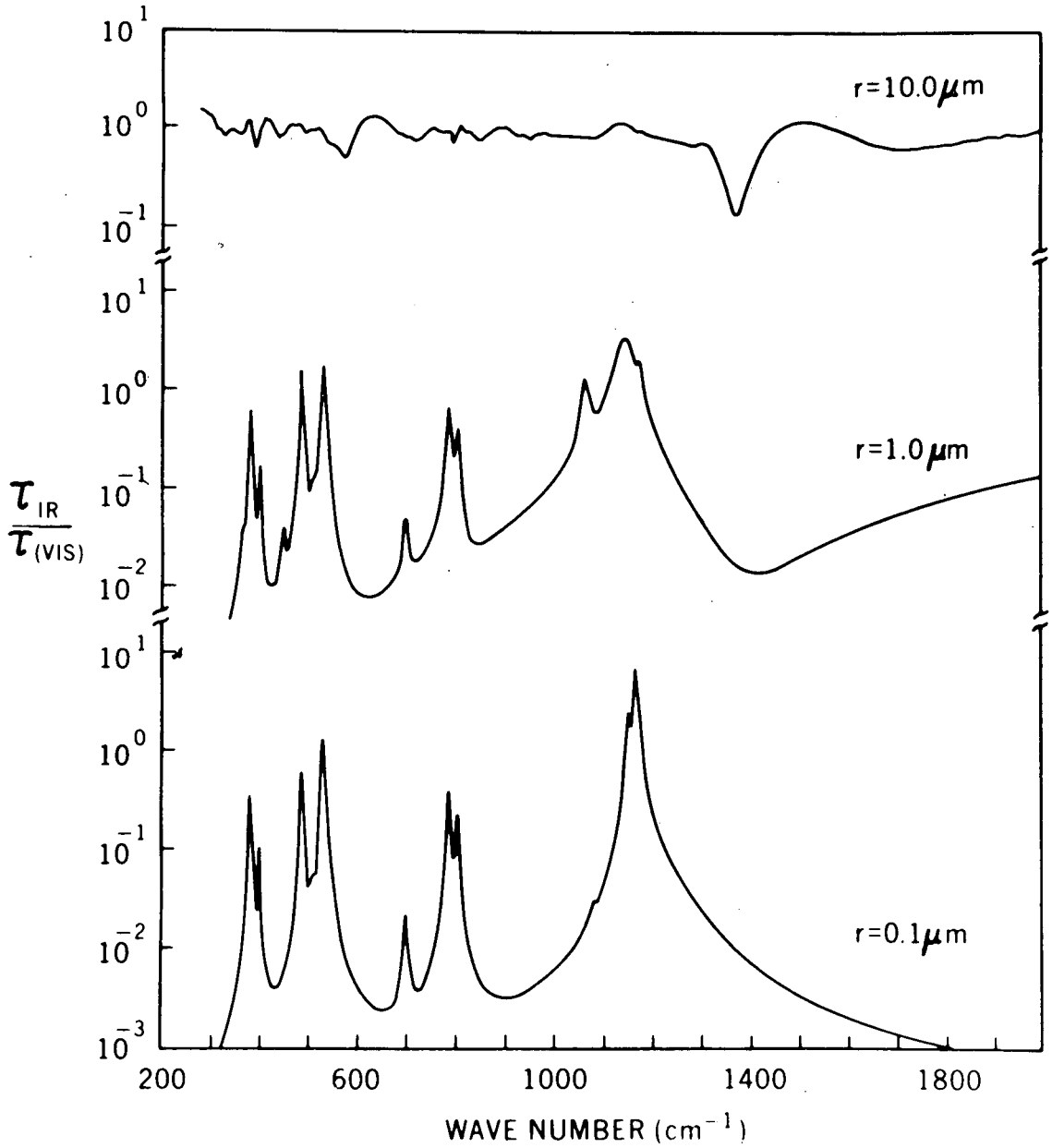

Figure 12. Ratios of infrared to visible optical depths (τ_{IR}/τ_{VIS}) for 0.1 μm, 1.0 μm, and 10.0 μm radius particles.

Finally, the absorption and scattering cross sections were used as input to a numerical solution of the equation of radiative transfer for a dust laden Martian atmosphere; the effects of molecular absorbers and emitters are not included. The radiative transfer calculations were normalized to a visible optical depth of unity, so that the integrated number of particles in a vertical column decreases as the dimensions of the particles increase (Table 4). The numerical solution accounts for the absorption and multiple scattering of the radiation by the dust in the atmosphere and the emission from both the lower bounding surface and the dust particles. Results of the radiative transfer calculations for five particle sizes are shown in Figure 13. For these calculations the surface was assumed to be at a temperature of 260°K, the atmospheric temperature distribution was that derived on revolution 20 at midlatitudes (Hanel et al., 1972c), and the particles were distributed exponentially with altitude assuming a scale height of 10 km. Many of the features observed in the optical depths of Figure 12 are noticeable in Figure 13, with the widths of the spectral features generally increasing with particle radius.

The most striking feature of these results is the strong dependence of the sharpness of the spectral features on particle size. A crude comparison of the sharpness of the features in the calculated brightness temperature spectra with those in measured dust cloud spectra such as the one shown in Figure 14 appears to favor particles having radii between 1.0 and 10.0 μm.

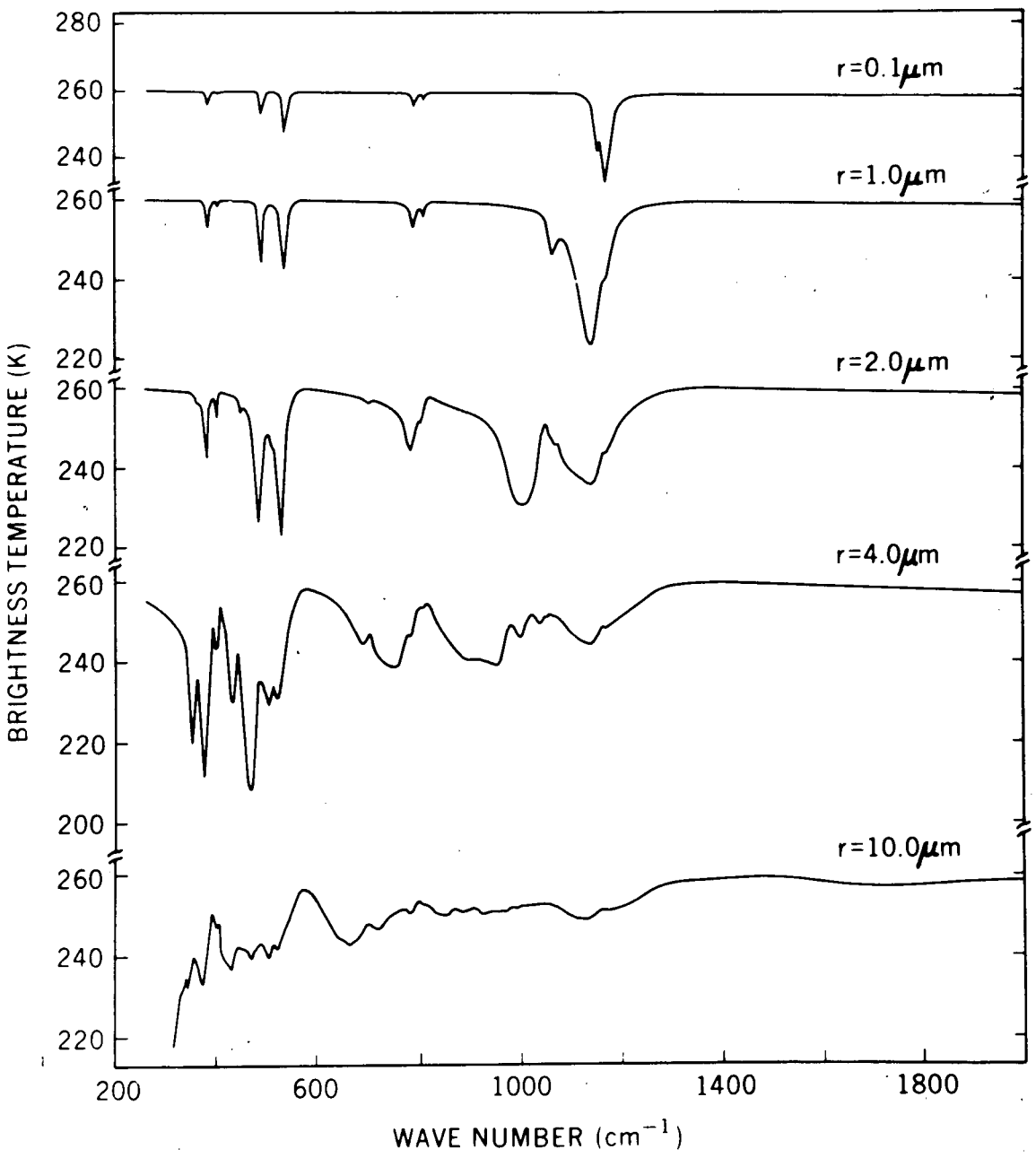

Figure 13. Synthetic brightness temperature spectra calculated for indicated particle sizes. The radiative transfer calculations include only the scattering and absorption effects of the particles and neglect the effects of gaseous molecular absorption.

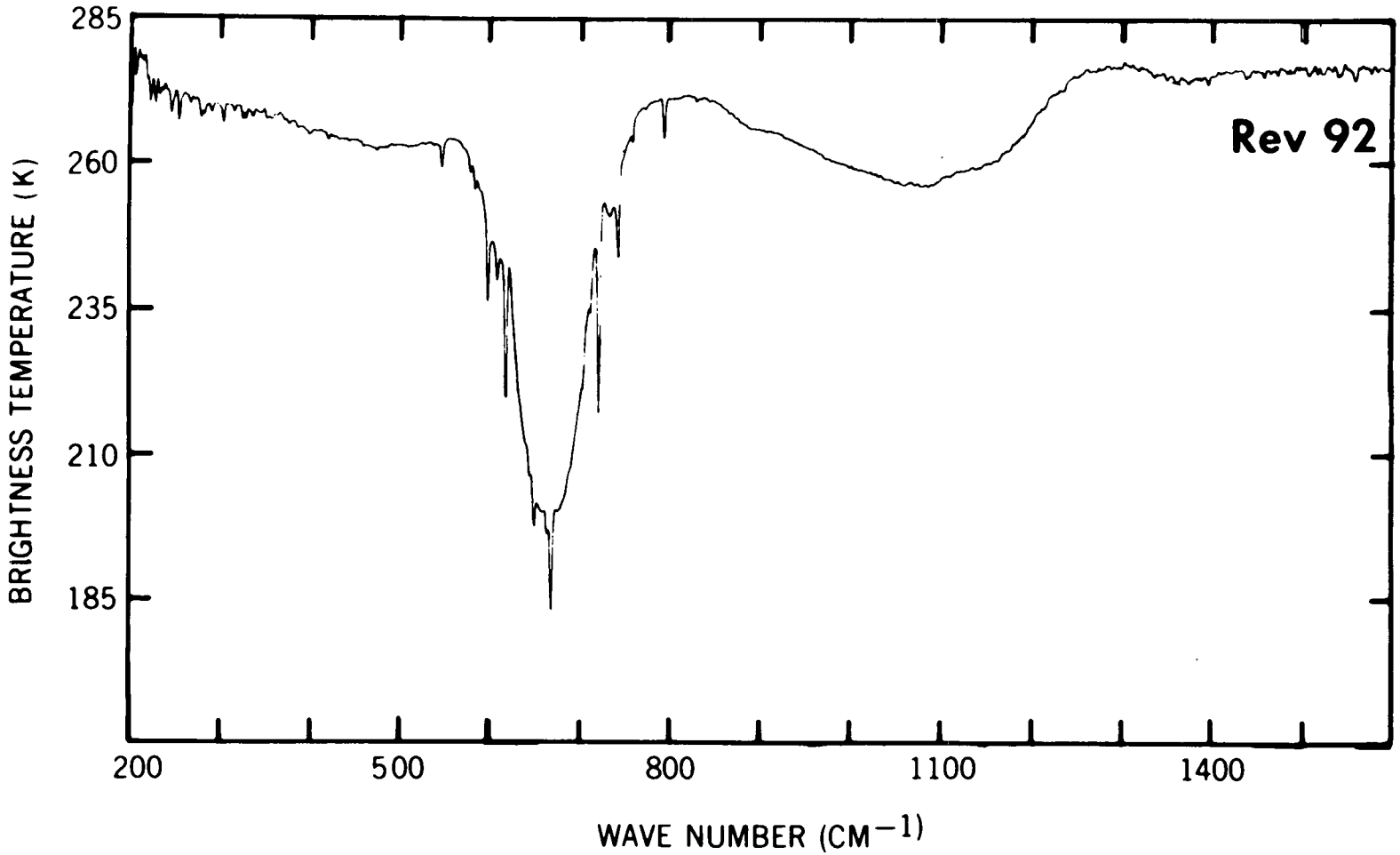

Figure 14. Measured brightness temperature spectrum from revolution 92 showing diffuse spectral features due to atmospheric dust.

Proceeding on the assumption that the dust in the Martian atmosphere is siliceous in nature, though not pure quartz, the radiative transfer modeling effort is being extended to include other minerals in the SiO_2 family. Effects due to broader particle size distributions are also being investigated. Present indications are that the correspondence between measured and calculated spectra will be improved by these efforts.

SUMMARY

This paper reports on recent progress in the interpretation of the thermal emission spectra of Mars. Improvements have been made in the CO_2 transmittances, which form the basis for determination of the surface pressure and atmospheric temperature profiles, and which must be well understood before a final analysis of minor gaseous constituents and of the mineral composition of the dust and of the surface can be made. Analysis of the water vapor distribution has revealed strong seasonal effects in the polar regions. By late southern summer ($L_s = 346°$, rev. 188) the atmospheric water vapor content over the South Polar Cap had dropped below 0.7 μm of precipitable water which is the saturation limit for the cold polar atmosphere. The wettest portion of the planet encountered during the orbital mission appears to be in the North Polar Cap region where saturated water vapor abundances of 20-30 μm were observed during Northern spring ($L_s = 60°$, rev. 528). Since the entire planet was not observed through a complete seasonal cycle and because of the interfering dust storm in the southern summer, it is not possible to infer from the

observed behavior of the water vapor distribution an imbalance in water vapor content between the northern and southern hemispheres. However, continued analysis of the water vapor distribution as a function of Martian season will contribute much to the understanding of polar phenomena and to the general surface-atmosphere interaction.

The analysis of the atmospheric pressure at the surface and of the topographic relief of Mars is proceeding from individual case studies to a global analysis. Even at low resolution, correlations between visual features and pressure variations are evident. Final analysis of pressures and topography await inclusion of improved CO_2 transmittances, corrections for diurnal pressure fluctuations, and corrections for distortions of the Martian geoid, as well as the use of a measured scale height instead of a constant value.

Inclusion of tidal theory in the analysis of atmospheric dynamics indicates that significant dirunal pressure fluctuations exist. During the dust storm diurnal pressure fluctuations occurred with a maximum near 0700 local time and -20° latitude and a minimum at 1900 hours and the same latitude. The calculated wind field near the surface shows a strong latitudinal as well as diurnal dependence. The surface boundary layer and surface topography are two important aspects which remain to be included in the model.

Using Mie theory and radiative transfer calculations, synthetic spectra of clouds of quartz spheres of various radii have been evaluated. Qualitative comparison of the computed spectra with measured spectra suggests that

particle radii were on the order of a few μm; if smaller particles dominated, rather sharp spectral features would be expected; substantially larger particles would have resulted in obscuration of the surface, even near the Christiansen frequency around 1300 cm^{-1}. Although the present models do not yet realistically parameterize the particle composition, size, or shape, refinements of the models promise to be useful for more specific identification of the Martian mineral dust composition and particle sizes.

ACKNOWLEDGEMENTS

Additional co-experimenters who have participated in the analysis of data from the Mariner 9 infrared spectroscopy experiment include W. Hovis, G. Levin, P. Lowman, C. Prabhakara, and P. Straat. W. Benedict, R. Drayson, and L. Kaplan have provided valuable contributions in the area of atmospheric transmittances. Discussions with C. Leovy and P. Gierasch were of value to the work on atmospheric circulation. Finally, the authors are indebted to the members of the Mariner 9 Project without whose efforts the experiment could not have succeeded.

REFERENCES

Barker, E.S., R.A. Schorn, A. Woszczyk, R.G. Full, and S.T. Little, Mars: Detection of Atmospheric Water Vapor During the Southern Hemisphere Spring and Summer Season, Science, 170, 1308-1310, 1970.

Benedict, W.S., Private Communication, 1970.

Drayson, S.R., Atmospheric Radiative Transfer by Carbon Dioxide, Proceedings of Conference on Atmospheric Radiation, Colorado State University, Fort Collins, Colorado, 77-79, 1972.

Handbook of Chemistry and Physics, Chemical Rubber Publishing Co., 1971.

Hanel, R.A., B.J. Conrath, W.A. Hovis, V. Kunde, P.D. Lowman, C. Prabhakara, and B. Schlachman, The Infrared Spectroscopy Experiment for Mariner Mars 1971, Icarus, 12, 48-62, 1971.

Hanel, R.A., B. Schlachman, E. Breihan, R. Bywaters, F. Chapman, M. Rhodes, D. Rodgers, and D. Vanous, The Mariner 9 Michelson Interferometer, Appl. Opt., 11, 2625, 1972a.

Hanel, R.A., B.J. Conrath, W.A. Hovis, V.G. Kunde, P.D. Lowman, J.C. Pearl, C. Prabhakara, and B. Schlachman, Infrared Spectroscopy Experiment on the Mariner 9 Mission: Preliminary Results, Science, 175, 305-308, 1972b.

Hanel, R., B. Conrath, W. Hovis, V. Kunde, P. Lowman, W. Maguire, J. Pearl, J. Pirraglia, C. Prabhakara, B. Schlachman, G. Levin P. Straat, and T. Burke, Investigation of the Martian Environment by Infrared Spectroscopy on Mariner 9; to be published in Icarus, 17, 1972c.

Kliore, A., Private Communication, 1972.

Kunde, V.G., Theoretical Molecular Absorption of CO in Late-type Atmospheres, Ap. J., 153, 435-449, 1968.

Lorell, J., G.H. Born, E.J. Christensen, J.F. Jordan, P.A. Laing, W.L. Martin, W.L. Sjogren, I.I. Shapiro, R.D. Reasenberg, and G. L. Slater, Mariner 9 Celestial Mechanics Experiment: Gravity Field and Pole Direction of Mars, Science, 175, 317-320, 1972.

Peterson, J.T., and J.A. Weinman, Optical Properties of Quartz Dust Particles at Infrared Wavelengths, J. Geophys. Res., 74, 6947-6952, 1969.

Spitzer, W.G., and D. A. Kleinman, Infrared Lattice Bands of Quartz, Phys. Rev., 121, 1324-1335, 1961.

Table 1

Lower and Upper Level Quantum Numbers (V_1, V_2, V_3, ℓ) and Corresponding Band Centers for Selected Isotopes of Carbon Dioxide

Lower Level	Upper Level	$O^{16}C^{12}O^{16}$	$O^{16}C^{13}O^{16}$	$O^{16}C^{12}O^{18}$	$O^{16}C^{12}O^{17}$	$O^{16}C^{13}O^{18}$
0000	0101	667.38	648.52	662.32	664.72	643.49
0101	0202	667.74	648.87	662.69	665.07	643.96
0101	1000	720.81	721.58	703.57	711.33	699.16
0101	0200	618.03	617.31	597.17	607.63	601.79
0202	0303	668.13	649.29	663.11	665.48	644.48
0200	0301	647.08	630.72	642.12	644.35	624.53
1000	1101	688.65	667.07	683.36	685.95	663.33
1101	1202	683.82	663.24	678.73	681.17	659.03
0202	1101	741.71	739.78	724.24	732.21	718.53
0202	0301	597.37	599.16	576.60	586.91	582.36

Table 2

Lower and Upper Level Quantum Numbers (V_1, V_2, V_3, ℓ) for Carbon Dioxide Identifications in the 15 μ Band

Wavenumber (cm^{-1})	Lower Level	Upper Level	Isotope ($O^{16}C^{12}O^{16}$ unless) otherwise listed)
544.28	1000	0301	
581.70	0303	0402	
597.34	0202	0301	
618.03	0101	0200	
643.49	0000	0101	$O^{16}C^{13}O^{18}$
648.52	0000	0101	$O^{16}C^{13}O^{16}$
662.32	0000	0101	$O^{16}C^{12}O^{18}$
667.38	0000	0101	
720.81	0101	1000	
741.74	0202	1101	
757.43	0303	1202	
770.36	0404	1303	
791.45	0200	1101	

Table 3

Surface and Water Vapor Parameters for Polar Regions

Earth Date	Revolution	Region	L_s	P_{Surf}	T_{Surf}	U_{Sat}	U_{obs}
11/29/71	30	South Polar Cap	301°	5 mb	186.0K	4200 μm	10-20 μm
1/11/72	116	South Polar Cap	326°	5 mb	181.8K	99 μm	15-25 μm
2/16/72	188	South Polar Cap	346°	5 mb	155.0K	0.7 μm	not detectable
1/4/72	102	North Polar Cap	322°	6 mb	145.0K	8 μm	not detectable
8/3/72	528	North Polar Cap	60°	6 mb	156.0K	30 μm	30 μm

Table 4

Vertically Integrated Column Number Density, N, and Column Mass Density, m, as Functions of Particle Radius, r, Assuming Unit Visible Optical Depth

r(μm)	N(cm^{-2})	m($gm\ cm^{-2}$)
0.1	7.04×10^{9}	7.79×10^{-5}
1.0	1.21×10^{7}	1.34×10^{-4}
2.0	3.38×10^{6}	2.98×10^{-4}
4.0	8.85×10^{5}	6.26×10^{-4}
10.0	1.50×10^{5}	1.66×10^{-3}

NASA–GSFC